EPS-476
Submitted to Pa 10,17 and Pl 1,2

# Jets and Energy Flow in $\gamma p$ collisions at HERA

H1 Collaboration

**Abstract:**

Properties of events with large transverse energy in the hadronic final state are analysed in photon-proton interactions. Comparisons of transverse energy distributions, jets and underlying event energy with different QCD calculations reveal the hadronic environment in $\gamma p$ collisions.

# 1 Introduction

The interactions of almost real photons and protons are the dominant scattering processes at the $ep$ collider HERA. A small fraction of these events have large transverse energy in the hadronic final state including the production of jets.

The main characteristics of these events are described by perturbative QCD calculations. Here the photon couples either directly to a parton of the proton (direct photoproduction), or indirectly via its own parton content (resolved photoproduction). Predictions for cross sections are obtained from the convolution of the matrix elements for the parton scattering and the parton distributions in the photon and the proton. Direct comparisons of measured cross sections with QCD calculations can – in principle – result in important conclusions on the parton scattering processes [1].

However, the comparisons of data and calculations revealed an environment for the jets which is not well described by QCD calculations [2, 3, 4]. Next to the jets, the measured energy flow – so called *underlying event* energy – was found to be far above the calculations. This underlying event energy is integrated into the measured jet energy and drastically changes the observed jet rates. Since many conclusions on the parton processes are essentially based on the comparison of measured jet cross sections and QCD calculations, general properties of photoproduction events need to be well understood.

In $\overline{p}p$ scattering the measured underlying event energy is also not well reproduced by QCD calculations using only the matrix elements and parton distributions [5]. However, the data could be described by adding interactions of the beam remnants to the calculations [6]. Similar improvements in the description of the photoproduction events were observed when interactions of the spectator partons were added to the calculations [4]. The photon offers here a unique probe for the study of the underlying event energy. Resolved photoproduction events can in principle have interactions between spectator partons of the proton and the photon. They can be compared with direct photoproduction events, which by definition can not have such additional interactions. Such comparisons reveal important information on the underlying event, as will be shown below.

In this paper detailed studies of photoproduction events with large transverse energy are presented in three topics:

1. How is transverse energy $E_t$ distributed: differential cross sections $d\sigma/dE_t$ and energy flow in the $\gamma p$ center of mass system (cms) are analysed, as well as the energy fraction which is contained in jets.

2. Properties of the underlying event: the energy density outside of jets is determined depending on the fraction of the photon energy which is available to the hard scattering process. Correlations of the transverse energy are measured.

3. Jet shape and rate: properties of jets are analysed depending on the jet energy. Jet cross sections are presented and the influence of the underlying event on the cross sections is studied.

## 2 Detector Description and Event Selection

A detailed description of the H1 apparatus can be found elsewhere [7]. The following briefly describes the components of the detector relevant for this analysis, which makes use of the calorimeters, the luminosity system and the central tracking detector.

The LAr calorimeter [8] extends over the polar angular range $4^\circ < \theta < 153^\circ$ with full azimuthal coverage, where $\theta$ is defined with respect to the proton beam direction ($+z$ axis). The calorimeter consists of an electromagnetic section with lead absorbers, corresponding to a depth of between 20 and 30 radiation lengths, and a hadronic section with steel absorbers. The total depth of the LAr calorimeter varies between 4.5 and 8 hadronic interaction lengths. The calorimeter is highly segmented in both sections with a total of around 45000 cells. The root mean square electronic noise per channel typically corresponds to 10 to 30 MeV. Test beam measurements of LAr calorimeter modules have demonstrated energy resolutions of $\sigma(E)/E \approx 0.12/\sqrt{E} \oplus 0.01$ with $E$ in GeV for electrons [9] and $\sigma(E)/E \approx 0.5/\sqrt{E} \oplus 0.02$ for charged pions [7, 10]. The hadronic energy scale and resolution have been verified from the balance of transverse momentum between hadronic jets and the scattered electron in deep inelastic scattering events and are known to a precision of 5% and 10% respectively.

The BEMC, with a thickness of 22.5 radiation lengths, covers the backward region of the detector, $151^\circ < \theta < 177^\circ$. A resolution of $0.10/\sqrt{E}$ with $E$ in GeV has been achieved for electrons. The BEMC energy scale is known to an accuracy of 1.7%.

The calorimeter is surrounded by a superconducting solenoid providing a uniform magnetic field of 1.15 T parallel to the beam axis in the tracking region. Charged particle tracks are measured in two concentric jet drift chamber modules (CJC), covering the polar angular range $15^\circ < \theta < 165^\circ$, and a forward tracking detector (FTD), covering the range $7^\circ < \theta < 25^\circ$.

The luminosity system consists of two TlCl/TlBr crystal calorimeters having a resolution of $\sigma(E)/E = 0.1/\sqrt{E}$ with $E$ in GeV. The electron tagger is located at $z = -33$ m and the photon detector at $z = -103$ m. The electron tagger accepts electrons with an energy fraction between 0.2 and 0.8 with respect to the beam energy and scattering angles below $\theta' \leq 5$ mrad ($\theta' = \pi - \theta$).

The events used in this analysis were taken during the 1993 running period, in which HERA collided 26.7 GeV electrons on 820 GeV protons. The scattered electron was measured in the electron detector of the luminosity system. The events were triggered by a coincidence of the electron tagger and of a single ray measured with the central proportional chambers. This minimum bias trigger was used for analysis without jet requirement. The corresponding data sample is later referred to as minimum bias data. For all jet analysis in the following sections in addition at least one track from the central jet chamber trigger was required. The integrated luminosity for events with (without) jet requirement corresponds to $290(117)\mathrm{nb}^{-1}$. Events were selected, if they fullfilled the following criteria:

1. The energy deposited in the electron tagger was in the range $8 \leq E_{tag} \leq 20$ GeV.

2. At least one track in the central tracker with transverse momentum above 0.3 GeV coming from the interaction region was required to determine the position of the vertex along the beam axis.

3. The width of the vertex distribution along the beam axis was approximately Gaussian with $\sigma = 10$ cm. Events were accepted, if they had a reconstructed vertex in the region $\pm 3\sigma$ around the nominal vertex position.

4. The events have either large transverse energy in the final state $E_t \geq 20$ GeV in the pseudo-rapidity range $-0.1 \leq \eta \leq 2.5$ (3254 events, used in sections 4.1, 4.2, 4.3 and 5.2), or at least one jet as defined below (3499 events, used in sections 5.1, 6.1 and 6.2). Background from non-*ep* scattering is negligable in both samples.

Throughout the paper the pseudo-rapidity $\eta = -\ln(\tan(\theta/2))$ is referred to as rapidity. Jet reconstruction was based on a purely calorimetric measurements using a cone algorithm [11] in a grid of cells in the azimuthal angle $\varphi^{cell}$ and rapidity $\eta^{cell}$ which extends from $-3 \leq \eta^{cell} \leq 3$. The cone radius $R = \sqrt{\Delta\eta^2 + \Delta\varphi^2}$ was chosen to be $R = 1.0$. Each jet has transverse energy above $E_t^{jet} \geq 7$ GeV and lies in the rapidity range $-1 \leq \eta^{jet} \leq 2.5$.

# 3 QCD generators

For comparisons with the data three different event generators were used. They are based on tree-level QCD matrix elements. All calculations were done with the same parton distributions: for the proton structure the GRV-LO [12] leading order parton density parametrizations were used, and for the photon structure the GRV-LO [13] leading order parametrizations. As will be seen below, the generators can be conceptually subdivided into calculations which include interactions of the beam remnants, and those which do not.

## 3.1 PYTHIA

The PYTHIA 5.7 event generator for photon-proton interactions [14] was used together with a generator for quasi-real photons. PYTHIA is based on leading order (LO) QCD matrix elements and includes models for the initial and final state parton radiation. The strong coupling constant $\alpha_s$ was calculated in first order QCD using $\Lambda_{QCD} = 200$ MeV with 4 flavours. The renormalization and factorization scales were both set to the transverse momentum $p_t$ produced in the parton-parton scattering. Since the QCD calculation of a single hard parton scattering is divergent for processes with small transverse momenta of the partons emerging from the hard interaction a lower cut-off has been applied in PYTHIA. This was set to $p_t \geq 2$ GeV.

PYTHIA allows for additional interactions within the same event [15]. These are LO QCD processes between partons from the photon remnant and partons from the proton remnant. This so called *multiple interaction* model has been explored in proton-antiproton collisions before [16, 17, 18]. A lower cut-off for the transverse momentum of the partons emerging from the multiple interaction processes has to be used in PYTHIA which was set to $p_t^{mi} \geq 1.2$ GeV. In the case of the multiple interactions an eikonalization scheme replaces the cut-off in $p_t$ for the hard scattering process. For the hadronization process the LUND fragmentation scheme was applied (JETSET [19]).

### 3.2 Herwig

The HERWIG 5.8 $ep$ generator is also based on LO QCD calculations [20]. It includes a parton shower model which allows for interference effects between the initial and final state showers (colour coherence) [21]. The renormalization and factorization scales were set according to the transverse momentum of the scattered partons with a cut-off at $p_t \geq 2\,\mathrm{GeV}$. $\alpha_s$ was calculated to first order using $\Lambda^{QCD} = 180\,\mathrm{MeV}$ for 5 flavours. A cluster model is used to simulate the hadronization effects [22].

Also HERWIG allows optionally for additional interactions of the beam remnants. These interactions are called *soft underlying event* and are modeled as 'soft' hadron-hadron collisions. After tuning, they are applied here for 35% of the resolved photon-proton interactions.

### 3.3 PHOJET

The PHOJET MC event generator is based on the two-component Dual Parton Model (DPM) [23] incorporating soft hadronic processes, described by the 'supercritical Pomeron', and hard processes, described by perturbative constituent scattering. The realization of the PHOJET generator is similar to the Monte Carlo event generator DTUJET [24] simulating multiparticle production in hadron collisions up to high energies. The hard processes are calculated with lower transverse momentum cutoff $p_t = 3\,\mathrm{GeV}$. The soft interaction is represented mainly by strings stretched between valence quark and antiquark and between quark and diquark of the colliding proton and resolved hadronic state of the photon. The transverse momenta of quarks at the ends of the strings ($p_t^{string}$) are assumed to be distributed according to $exp(-\beta \cdot p_t)$. The $p_t^{string}$ distribution is required to match the transverse momentum distribution of partons from hard processes at the scale of $p_t$. The characteristic feature of this model is multiple interactions. The multiplicities of soft and hard interactions are calculated within a unitarization scheme [25]. The average multiplicity in the energy range of HERA is estimated to be about 1.7 interactions per event. The details concerning the calculation of cross sections for different configurations of the final state are given in [26]. The Lund model as implemented in JETSET [19] is used for fragmentation.

## 4 Events with high transverse energy

### 4.1 Transverse energy cross section

Cross sections of the total transverse event energy $E_t$ have been previously measured in $\gamma p$ [27] and $\overline{p}p$ scattering at different cms energies [28, 30, 31]. The distributions are steeply falling in the region of minimum bias events and tend to flatten towards large transverse energy depositions. For sufficiently high $E_t$ the distributions can be equally well described by a power law $(E_t)^{-n}$ or an exponential decrease $\exp(-\lambda E_t)$. With increasing cms energies $\sqrt{s_{\overline{p}p}}$ the slope $\lambda$ at large $E_t$ is found to decrease as $\lambda = a/\sqrt{s_{\overline{p}p}}$ with $a \approx 40$.

In Fig.1a the differential $ep$ cross section $d\sigma/dE_t$ is shown. For this analysis the event sample with the large $E_t$ requirement was used. The transverse energy has been integrated in the cms rapidity range $-2.5 \leq \eta^* \leq 1$, where $\eta - \eta^* = 0.5 \ln(E_p/E_\gamma) \sim 2$. The measurement corresponds to scaled photon energies between $0.3 \leq y \leq 0.7$ and negative squared momentum transfer $Q^2 \leq 0.01\,\mathrm{GeV}^2$.

Corrections of the observed transverse energy are parametrized as a function of the rapidity of the energy deposits. The corrections increase with rapidity and amount to $0.8 - 1.2$. The parametrization shows a slight dependence on the Monte Carlo model which contributes with 10% to the systematic error. Acceptance effects of the electron tagger were corrected and contribute with 5% to the systematic error. This error also includes the uncertainty of the luminosity measurement. The determination of the minimum bias trigger efficiency has a 2% error. The dominant systematic error comes from the uncertainty in the knowledge of the LAr calorimeter energy scale which contributes an error of $1\% \times E_t$, with $E_t$ in GeV.

The differential cross section is well described by calculations of the PHOJET generator (Fig.1a full line). The calculation of the PYTHIA generator without multiple interactions (dashed line) gives too small values of the cross section.

The shape of the measured differential $E_t$ cross section can be described by a power law with $n = 5.9 \pm 0.1$. The power $n$ is similar to that of the transverse energy jet cross section shown below which is consistent with underlying hard parton scattering processes. The slope of the exponential fit gives $\lambda = 0.21 \pm 0.01$ respectively $a = 42$ at $\sqrt{s_{\gamma p}} = 200\,\mathrm{GeV}$. This value compares well with the energy dependence found in $\overline{p}p$ scattering and underlines the similarity of $\gamma p$ and $\overline{p}p$ scattering at large cms energies.

### 4.2 Transverse energy flow

The peripheral scattering of two hadrons results in a transverse energy flow which can be described by a rapidity plateau of width $2\ln(\sqrt{s}/m)$, with final state hadrons of mass $m$ carrying transverse momenta around $p_t \sim 300\,\mathrm{MeV}$ and $\sqrt{s}$ refering to the cms energy [29]. In Fig.1b the average transverse energy flow in photoproduction events is shown versus the $\gamma p$ cms rapidity. The distributions are corrected for detector effects. The open points refer to minimum bias data. As expected from peripheral scattering of a hadron like photon and a proton the data exhibit a plateau within the rapidity interval shown.

The full points refer to large $E_t$ events with corrected total transverse energies between $25\,\mathrm{GeV} \leq E_t(-2.5 \leq \eta^* \leq 1) \leq 30\,\mathrm{GeV}$. The distribution is incompatible with being flat and has a maximum around $\eta^* = 0$ in the $\gamma p$ cms.

Similar distributions have been observed in $\overline{p}p$ scattering with large transverse energy in the final state. Here the $E_t$ distribution versus rapidity is centered on the cms rapidity $\eta^* = 0$ and

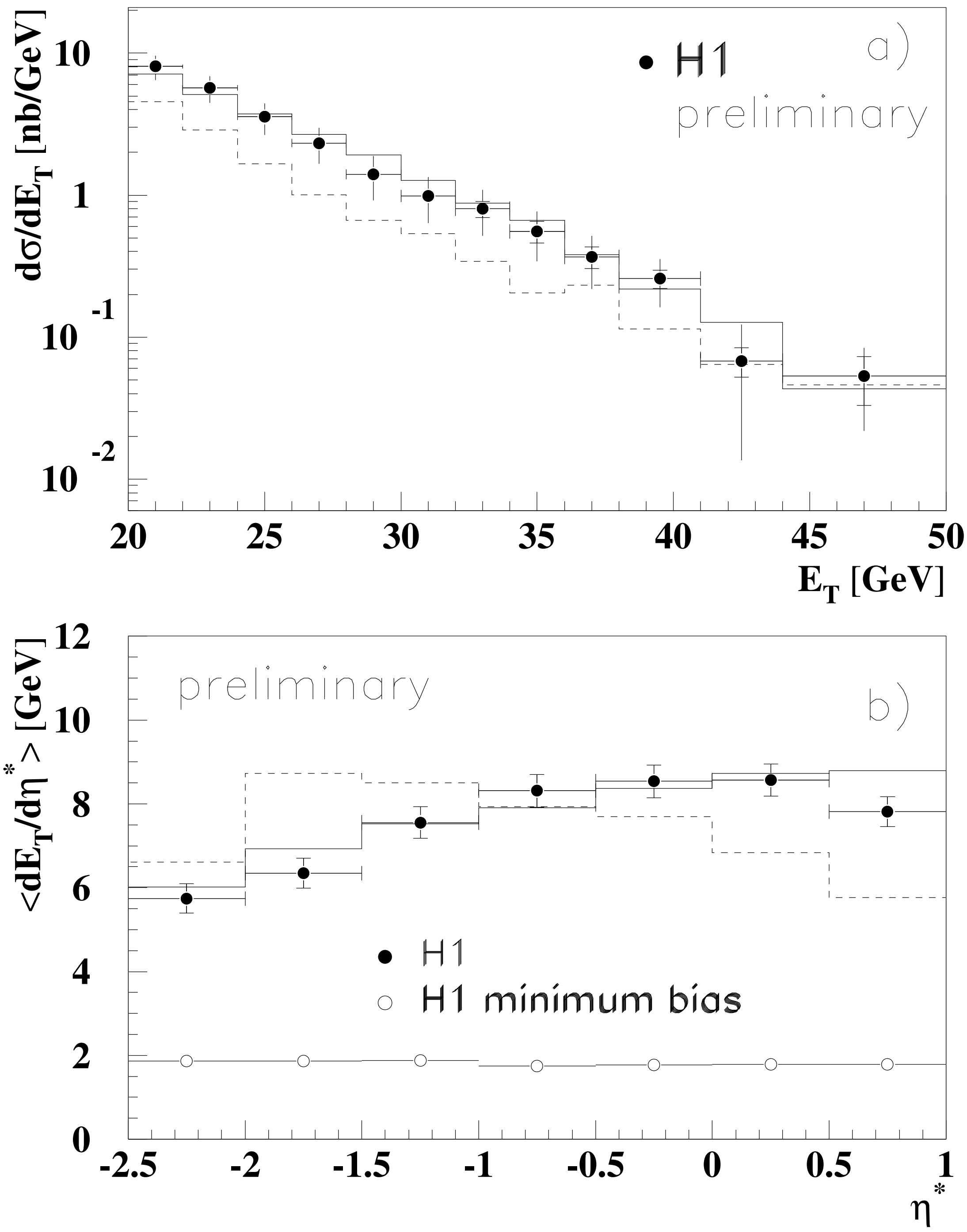


**Figure** 1: a) Differential transverse energy cross section integrated in the rapidity interval $-2.5 \leq \eta^* \leq 1$. Full points are data, the inner error bars are statistical, the outer error bars are the quadratic sum of statistical and systematic errors. The full/dashed curve are calculations of QCD models with (PHOJET)/without (PYTHIA) interactions of the beam remnants. b) Transverse energy flow per event versus the rapidity in the $\gamma p$ cms. Full points refer to corrected total transverse energies between $25\,\mathrm{GeV} \leq E_t(-2.5 \leq \eta^* \leq 1) \leq 30\,\mathrm{GeV}$. Open points refer to minimum bias data. Only statistical error bars are show.

has e.g. at $\sqrt{s_{\overline{p}p}} = 630\,\mathrm{GeV}$ a half width of the half maximum of only one unit of rapidity instead of a possible total plateau width of $\Delta\eta \sim 13$ (using the proton mass) [30].

In the picture of parton-parton scattering processes a symmetric energy flow around $\eta^* = 0$ is expected, if the distribution is dominated by processes with on average equal momentum fractions of the parton from the photon and that of the proton $< x_\gamma > \sim < x_p >$. With respect to the different quark distributions of the proton and the photon the measured energy flow would then require a large gluon component in the photon which is disfavoured [4]. Another possibility is the superposition of hard parton-parton and remnant-remnant interactions where the latter deposits energy predominantly in the central rapidity region.

The full points in Fig.1b are compared with several calculations: PYTHIA without multiple interactions (dashed) shows an assymmetric distribution with respect to the $\gamma p$ cms, centered in the photon hemisphere. This is expected from different parton distributions in the photon and the proton $< x_\gamma > \geq < x_p >$. PHOJET (full), which includes interactions of the beam remnants, has a maximum close to the central region.

### 4.3 Jet rate

In tree level QCD calculations two partons emerge from a hard scattering process, each fragmenting into a jet. The jet multiplicity which is finally measured, however, depends on the jet definition which is here a cone algorithm with cone size $R = 1$, a jet transverse energy threshold $E_{t,min}^{jet}$, and the total transverse energy in the event.

In Fig.2 the relative rate of jet multiplicities $n_{jet}$ is shown as a function of the observed transverse event energy $E_t^{vis}$. These results are based on the event sample with large $E_t$ in the final state. The visible jet energy threshold is set to $E_{t,min}^{jet} = 7\,\mathrm{GeV}$ with the jet axis between $-2.5 \leq \eta^* \leq 0.5$. The transverse event energy is calculated within the rapidity interval $-3 \leq \eta^* \leq 1$.

At $E_t^{vis} = 20\,\mathrm{GeV}$ 70% of the events have no jets at all above this threshold. While at $E_t^{vis} = 35\,\mathrm{GeV}$ half of the events contain two jets as expected from the tree level QCD picture. At $E_t^{vis} = 40\,\mathrm{GeV}$ 10% three jet events are observed, showing the effect of higher order processes with possible contribution of the photon remnant. Here the rate of events without jets has essentially vanished.

The average fraction of the event energy which is contained in jets can be estimated from the sum of the jet rates times the jet energies. At $E_t^{vis} = 20\,\mathrm{GeV}$ the average energy per event resulting in jets with the chosen parameters accounts to $\sim 10\%$ of the total visible energy. At $E_t^{vis} = 40\,\mathrm{GeV}$ about half of the event energy is contained in jets. The jet rates are reasonably described by calculations of the PYTHIA generator (Fig.2) with multiple interactions, which include here a detailed simulation of the detector effects.

### Summary

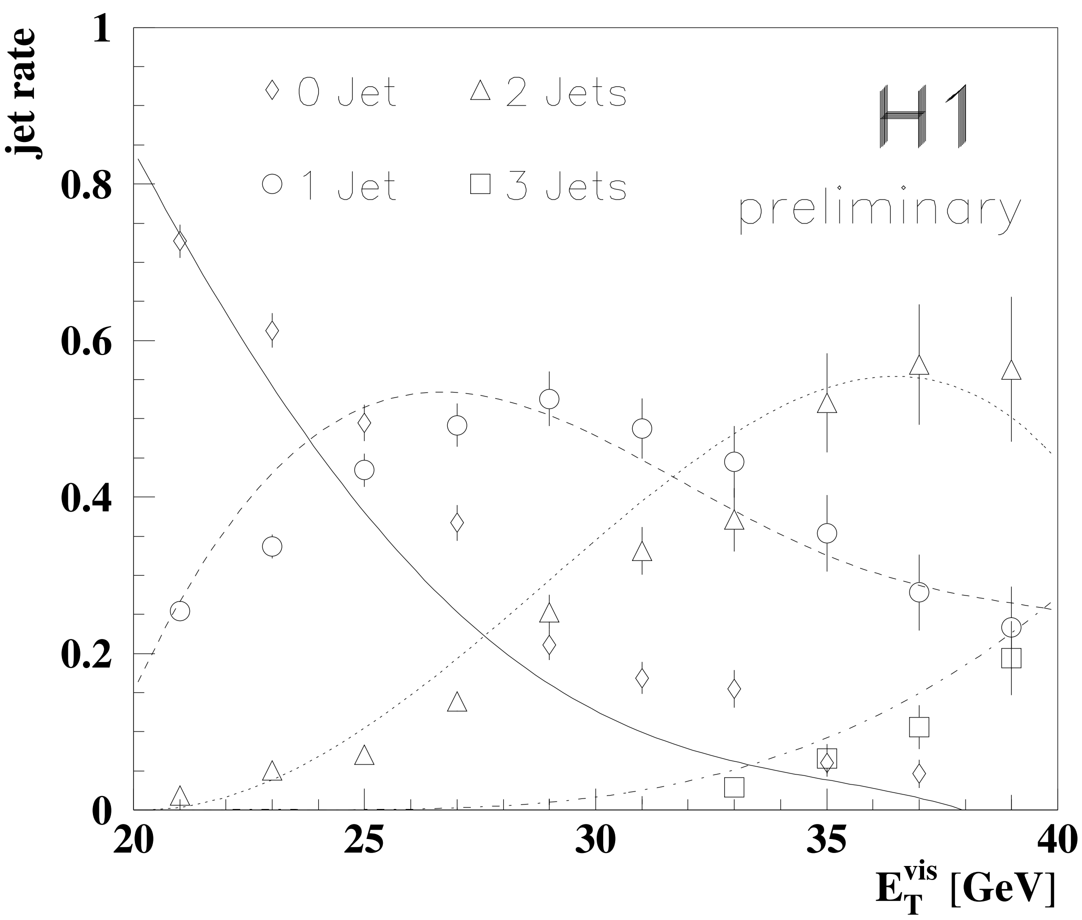


**Figure** 2: Relative rate of 0=diamonds, 1=circles, 2=triangles, 3=squares jet events versus the observed transverse energy collected in the rapidity range $-3 \leq \eta^* \leq 1$. The observed jet energies $E_t^{jet}$ are above 7 GeV summed in a cone of size $R = 1$ for jet axes between $-2.5 \leq \eta^* \leq 0.5$. Symbols are data with only statistical error bars shown. The curves are calculations of a QCD generator including interactions of the beam remnants (PYTHIA).

The energy distributions of the photoproduction data are very similar to those measured in $\overline{p}p$ scattering: the slowly decreasing transverse energy spectrum, the rapidity distribution which is not flat, and the multijet production demonstrate the scattering of constituents of the photon and proton. Comparisons of the data with different generators – which are based on LO QCD matrix elements plus parton showers – show that models which include interactions between the beam remnants provide better descriptions of the data than models without such a mechanism.

# 5 Underlying event energy

## 5.1 Transverse energy density outside of jets

In the framework of QCD the energy flow around a jet axis can be divided into two components [5]:

A.) Transverse energy of the partons that participate in the hard scattering including initial and final radiation from these partons, plus hadronization effects,

B.) Transverse energy from the interactions of the spectator partons which is essentially uncorrelated with the hard scattering process, plus hadronization effects.

Monte Carlo generators which include both components describe distributions of the hadronic final state in $\overline{p}p$ [6] and $\gamma p$ ([4] and this paper) scattering remarkably better than generators including only the effects of the hard parton interaction (item A). On the existence of hard spectator interactions (item B) only limits exist so far from an analysis of multi-jet events [16].

At HERA the photon offers a unique probe to study the transverse energy flow outside of jets, the underlying event (also 'jet pedestal'). Within a partonic picture of the $\gamma p$ interactions with *resolved* photons the underlying event should contain apart from hadronization effects

1. Transverse energy from QCD radiation off the initial state partons from the photon and the proton side, which will undergo a hard scattering,
2. Transverse energy from QCD radiation off the final state hard scattered partons,
3. Transverse energy of spectator interactions which is not correlated with the hard parton scattering process, and
4. Transverse energy of non-interacting spectator partons which is also uncorrelated with the hard parton scattering process.

*Direct* $\gamma p$ interactions, however, do not have initial state QCD radiation off a parton from the photon side (item 1) and can neither have interactions of the spectator partons (item 3), nor show a photon remnant (item 4). They should, however, have the same final state radiation (item 2) as the resolved photon interactions. The different contributions can therefore partly be disentangled by studying the underlying event as a function of, e.g., the parton momentum from the photon side which should be 1 for direct photon interactions and less than 1 in the case of resolved photon interactions.

In tree-level QCD calculations the momentum fraction of the parton from the photon can be estimated from

$$x_\gamma^{jets} = \frac{E_t^{jet1} e^{-\eta^{jet1}} + E_t^{jet2} e^{-\eta^{jet2}}}{2E_\gamma}. \tag{1}$$

In this analysis the jet event sample is used, requiring at least two jets. $x_\gamma^{jets}$ is reconstructed using the two jets with the highest transverse energy $E_t^{jet}$ in the event and their rapidities $\eta^{jet}$. The energy of the photon $E_\gamma$ is determined from the energy measured in the electron tagger. The resolution of $x_\gamma^{jets}$ is between $15-30\%$, getting worse from 0 to 1.

The transverse energy is summed in the central $\gamma p$ collision region $-1 \leq \eta^* \leq 1$. Energy deposited around the two jet axes within $R = \sqrt{(\Delta\varphi)^2 + \Delta\eta^2)} \leq 1.3$ is excluded from the energy summation. The *transverse energy density* $< E_t > /\Delta\eta/\Delta\varphi$ is then defined as the event average energy sum $< E_t >$ per unit area in the $(\eta, \varphi)$ space. In Fig.3 the transverse energy density $< E_t > /\Delta\eta/\Delta\varphi$ (points) is shown for the central $\gamma p$ collision region. This distribution rises towards small values of $x_\gamma^{jets}$.

Systematic errors originate from the following sources: the correction of the measured energy was parametrized depending on the rapidity of the energy deposit. The parametrization depends slightly on the Monte Carlo model which contributes 10% to the systematic error. Migration effects in $x_\gamma^{jets}$ were determined with different generator models and are uncertain to the level of 14%. These errors are shown in Fig.3. In addition, the uncertainty in the knowledge of the hadronic energy scale of the LAr calorimeter may change the overall normalization of the energy density by 5%. Other sources of systematic errors have a negligable influence on the result.

The long-dashed line indicates the energy density found in minimum bias events where $x_\gamma^{jets}$ is not measureable. The energy density for directly interacting photons ($x_\gamma^{jets} = 1$) is found to be close to the energy density found in minimum bias events. That means, neither the initial state radiation effects of the parton from the proton, nor the final state radiation effects can be large. The energy density is mainly influenced by effects of the hadronization phase.

At small $x_\gamma^{jets}$, initial state radiation off the parton from the photon side can, in principle, increase the energy density. However, the parton momentum fraction $x_\gamma$ at the hard scattering process is in average much larger than the momentum fraction of the parton from the proton $x_p$. So there should be even less radiation off the parton from the photon compared to the radiation off the parton from the proton.

The measured energy density, however, increases by 0.6 GeV/rad to 3.5 times the minimum bias energy density, which indicates an additional component in the data beyond QCD radiation effects. A natural explanation for this additional energy flow are interactions between the parton spectators (item 3): the probability for these additional interactions increases with the energy of the photon remnant.

The energy density in minimum bias and jet events has been studied before in $\overline{p}p$ scattering at different cms energies [33, 5]. For the minimum bias events the $\overline{p}p$ results of the energy density

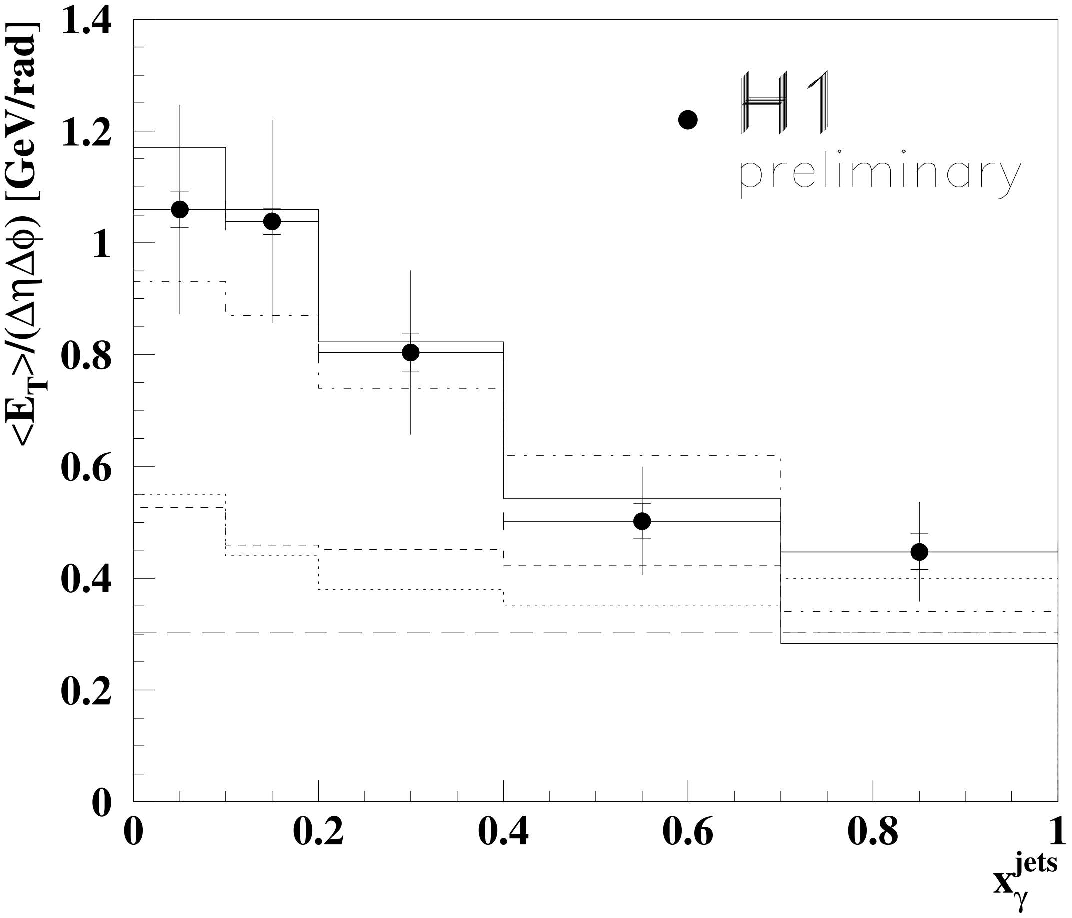


**Figure** 3: Transverse energy flow in the central photon-proton collision region ($-1 \leq \eta^* \leq 1$) outside of the two jets with the highest $E_t^{jet}$ per event and unit area in rapidity. $x_\gamma^{jets}$ is a measure of the momentum fraction of the parton from the photon side. Circles are data, the inner error bars are statistical, the outer error bars result from the quadratic sum of statistical and systematic errors. An overall uncertainty in the hadronic energy scale of 5% is not shown in the figure. The long-dashed line indicates the energy density measured in minimum bias events. The histograms show the calculations of different QCD generators with/without interactions of the beam remnants (full=PHOJET, dash-dotted=PYTHIA)/(dotted=HERWIG, short-dashed=PYTHIA).

together with the $\gamma p$ result fit well into a dependence of $< E_t > /\Delta\eta/\Delta\varphi$ on the logarithm of the cms energy. A similar increase of the energy density with the cms energy is found in jet events using the results from $\overline{p}p$ scattering and from $\gamma p$ interactions below $x_\gamma^{jets} \leq 0.1$.

Also shown in Fig.3 are the results of different Monte Carlo generators. The short-dashed histogram refers to the PYTHIA calculation without multiple interactions. This calculation is compatible with the measured energy density at large $x_\gamma^{jets}$, but shows only a small increase towards $x_\gamma^{jets} = 0$, as one may expect from increased initial state radiation effects. The use of another parametrization of the photon structure function, e.g. LAC1 [34], does not change this result. The HERWIG generator gives similar results (dotted histogram). Instead the calculations of the PHOJET generator (full histogram) and PYTHIA with multiple interactions (dash-dotted histogram) provide reasonable descriptions of the data. Both models include interactions between the photon and proton spectator partons and influence only the central $\gamma p$ collision region.

For the first time the underlying event energy has been measured in jet events using direct and resolved photon probes. The steep rise of the energy density in the central $\gamma p$ collision region between direct and hadron like photons and the comparisons with different Monte Carlo models demonstrate the need for an additional component beyond a two parton scattering process.

### 5.2 Transverse energy correlations

Energy-energy correlations are sensitive measures of how energy is distributed over the available phase space. Here the aim is to gain information on the transverse event energy measured in Fig.1 and in jet events (Fig.3). A study of the rapidity correlations relative to the central $\gamma p$ collision region, where the event energy is largest, should reveal information on the underlying event and provide important tests of the models which describe the average event energy correctly.

In Fig.4 rapidity correlations $\Omega$ are shown with respect to the cms rapidity $\eta^* = 0$ for events with large transverse energy in the final state. Energy of jets is included in this measurement. The correlations have been calculated using

$$\Omega(\eta^*) = \frac{1}{N_{ev}} \sum_{i=1}^{N_{ev}} \frac{(< E_{t,\eta^*=0} > - E_{t,\eta^*=0})_i \, (< E_{t,\eta^*} > - E_{t,\eta^*})_i}{(E_t^2)_i} \tag{2}$$

The average value of the transverse energy in a bin $< E_{t,\eta^*} >_i$ has been determined with all events in the sample.

The data distribution (full points) shows short range correlations around the $\gamma p$ cms reference bin. Long range anti-correlations are observed in the photon hemisphere which have a minimum around $\eta^* = -1.8$ and dissappear around $\eta^* \approx -3$.

The dashed histogram in Fig.4 shows the calculation of the PYTHIA generator without multiple interactions, including a detailed simulation of the detector effects. The correlations have the same shape, but the (anti-) correlation is twice as strong as observed in the data. That means, too much energy in the central $\gamma p$ collision region is correlated with the other energy deposited in the event. The PYTHIA version including multiple interactions is shown in Fig.4

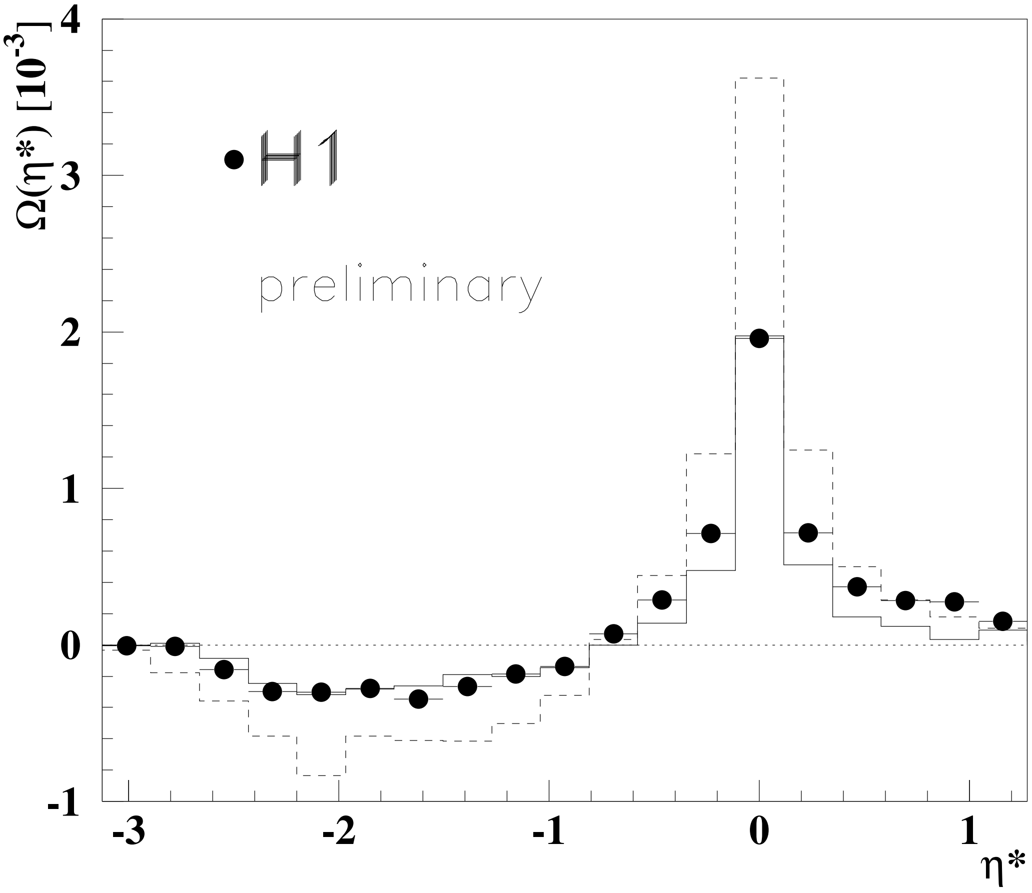


**Figure** 4: Observed rapidity correlations with respect to the central $\gamma p$ collision region $\eta^* = 0$. Full points are data, only statistical error bars are shown. The full/dashed histogram represents a calculation of a QCD generator (PYTHIA) with/without interactions of the beam remnants.

as full histogram. Here event energy is added around $\eta^* = 0$ which stems from interactions of the spectator partons and is not correlated with the major part of the event energy which results from the hard scattering process. Although the model gives no perfect description of the data, it is demonstrated that the addition of uncorrelated energy into the events results not only in the correct average underlying event energy (Fig.3), but also gives the correct correlation strength (Fig.4). The same conclusions hold for events including jets.

**Summary**

The comparison of the underlying event in $\gamma p$ collisions with direct and hadron like photons shows large differences in the transverse energy density. In the central $\gamma p$ collision region, processes where large fractions $x_\gamma \sim 1$ of the photon energy are carried into the hard scattering process have a similar energy density as minimum bias events. Processes with resolved photons $x_\gamma \sim 0$ are found to have 3.5 times the energy of minimum bias events. This increase is by far larger than expected from QCD generators using LO QCD matrix elements plus parton showers, but can well be explained by models including remnant-remnant interactions. In addition, comparisons of the measured energy-energy correlations with different models demonstrate that the additional energy of remnant-remnant interactions decreases the correlation strength to the level observed in the data.

Therefore, the underlying event in photoproduction events can be consistently interpreted as the energy sum of the hard scattering process plus interactions of the beam spectators. Both components are connected by the momentum fraction of the parton from the photon side which determines the energy in the hard interaction and the energy left for interactions of the two beam remnants.

# 6 Properties of jets and jet cross sections

## 6.1 Jet shape

The transverse energy distribution around a jet axis shows an approximately Gaussian shape. In perturbative QCD the jet width is expected to decrease depending on the jet energy [37].

In Fig.5a the observed transverse energy flow in the azimuthal angle $|\Delta\varphi|$ around the jet with the highest $E_t^{jet}$ in events with at least 2 jets is shown. The jets were found in the photon hemisphere between $-2 \leq \eta^*_{jet} \leq -1$ and have transverse energies between $9 \leq E_t^{jet} \leq 11$ GeV summed in a cone of size $R = 1$. The energy flow has been integrated in a slice of $|\eta^{cell} - \eta^{jet}| \leq 1$ around the jet axis. The two jets usually deviate from a back-to-back configuration in the azimuthal angle. The axis of the second jet in Fig.5a had to be between $-\pi \leq \Delta\varphi \leq 0$: since the jets have a total width of approximately two units in rapidity, the region $1 \leq \Delta\varphi \leq 2$ is essentially free of the second jet and shows the underlying event energy.

The full curve in Fig.5a represents an empirical 3 parameter fit of the jet profile using a function closely related to a Gaussian curve:

$$f(\Delta\varphi) \quad = \quad A \exp\left(-(\sqrt{\Delta\varphi} + b)^4 + b^4\right) + P \qquad (3)$$

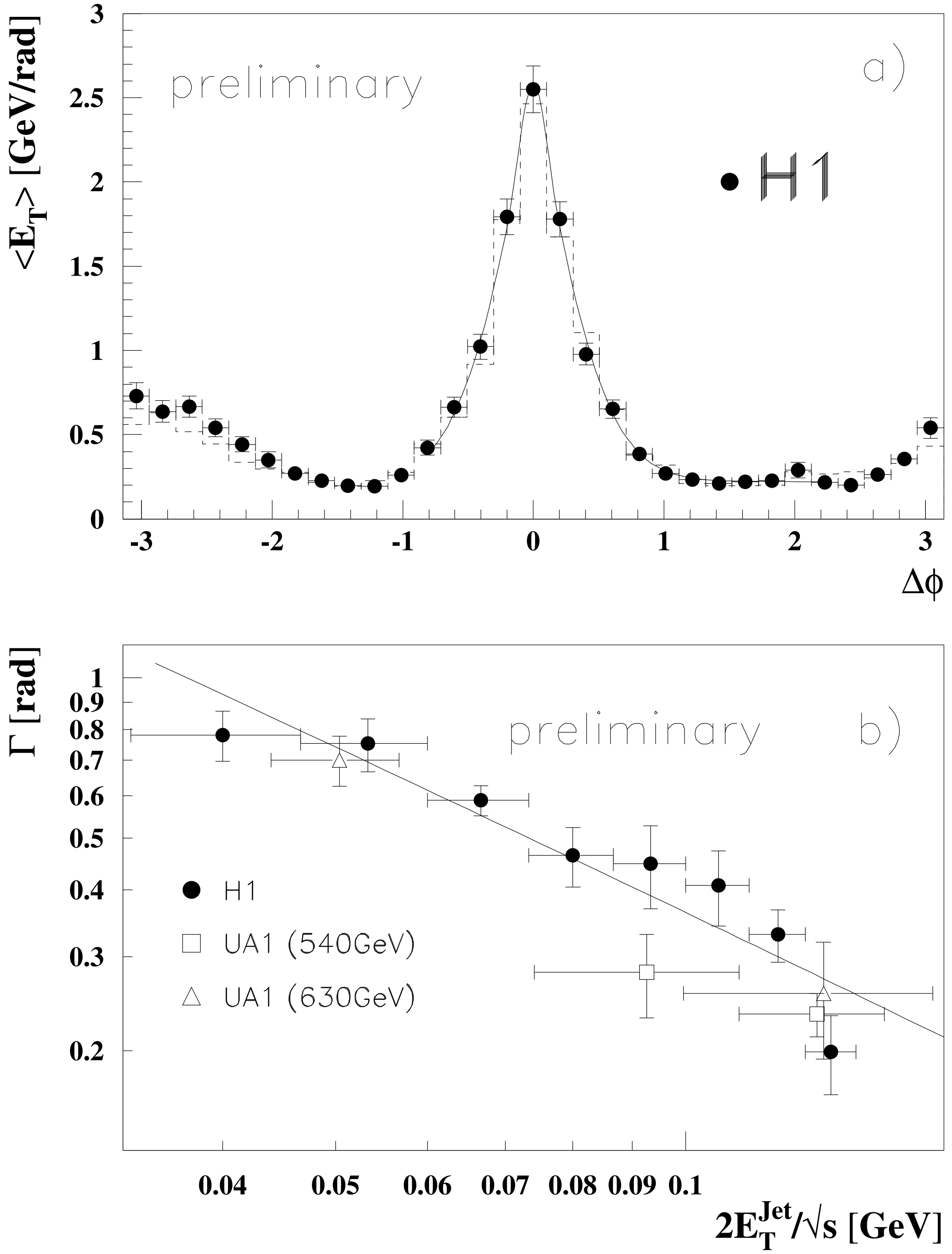


**Figure** 5: a) Observed transverse energy around the jet axis is shown versus the azimuthal angle $\Delta\varphi$ for jets in the photon hemisphere $-2 \leq \eta^*_{jet} \leq -1$ and $9 \leq E_t^{jet} \leq 11$ GeV. The points represent the data with their statistical error bars. The axis of the second jet is between $-\pi \leq \Delta\varphi \leq 0$. The histogram is a calculation of a QCD generator (PYTHIA), and the curve is a fit using (3). b) The fitted full width $\Gamma$ at half maximum above the underlying event of a jet is shown depending on the scaled jet energy $2E_t^{jet}/\sqrt{s_{ep}}$, where the $ep$ center of mass energy is used following [37]. Points are H1 $\gamma p$ data, the inner error bars are the statistical errors of the fits, the outer error bars represent the quadratic sum of the statistical and systematic errors. Open symbols are derived from fits to jet profiles of $\overline{p}p$ data using the cms energies $\sqrt{s_{\overline{p}p}}$ [33, 35]. The full line represents a QCD inspired fit to the $\gamma p$ data.

Parameter $A$ describes the amplitude of the jet at $\Delta\varphi = 0$ which is mainly constraint by the energy measured in the central bin. $P$ reflects the underlying event energy (pedestal). The full width half maximum above the pedestal is then $\Gamma = 2((\ln 2 + b^4)^{1/4} - b)^2$. Regions potentially affected by the second jet are excluded from the fit.

In Fig.5b the width $\Gamma$ of jets from $\gamma p$ interactions (full points) is shown as a function of the scaled transverse jet energy $2E_t^{jet}/\sqrt{s_{ep}}$. Here the $ep$ cms energy is used, following QCD calculations of jet shapes [37]. The decrease of $\Gamma$ for jet energies between $5 \leq E_t^{jet} \leq 20\,\mathrm{GeV}$ is cleary seen. This effect is well described by the QCD generators. It can be described, e.g., by a dependence on $1/E_t^{jet}$ which is expected from the QCD calculations. The jet pedestal has – in this rapidity region – no dependence on $E_t^{jet}$, and the amplitude varies as a function of $E_t^{jet}$ and $\Gamma$. Systematic errors are dominated by the choice of the $\Delta\varphi$ interval used for the fit ($\leq 10\%$).

In the same Fig.5b the photoproduction data are compared with results from fits to jet profiles of $\overline{p}p$ data at different cms energies (open symbols) [33, 35]. Here rapidity projections of the jet profiles were used, allowing $P$ in (3) to depend linearily on the rapidity. The same jet width as in $\gamma p$ data is found in $\overline{p}p$ data at different jet energies. Within error bars the jet width measured in $\gamma p$ and $\overline{p}p$ correspond via the ratio of the jet energy and the cms energy. Such universal jet shapes are expected from QCD calculations, except for a small modification due to the running of the strong coupling constant $\alpha_s$ [37] (here 15%).

Therefore, jets resulting from $\gamma p$ collisions show the shape, and narrowing of the jet width with increasing $E_t^{jet}$, as expected from QCD calculations. These jets are of the same nature as the jets observed in $\overline{p}p$ scattering.

### 6.2 Jet cross sections

Differential inclusive jet cross sections have been measured in photoproduction events at HERA before [2, 3]. The transverse energy cross section $d\sigma/dE_t^{jet}$ is steeply falling and can well be described by a power law $(E_t^{jet})^{-n}$. Such a falling distribution is expected from QCD calculations. Here the matrix elements of different parton scattering processes (quark-gluon, gluon-gluon etc.) are summed according to the quark and gluon distributions in the photon and the proton. The calculations are only modestly sensitiv to the parton distributions, but reflect essentially the features of the matrix elements. The measured cross section can well be described by these calculations and can therefore be interpreted as the result of underlying parton scattering processes. The observed jets are mainly located in the photon hemisphere and cover there several units in rapidity. Jet rapidity cross sections $d\sigma/d\eta^{jet}$ are therefore sensitiv to the parton distributions in the photon. These parton distributions can be extracted by comparison with QCD calculations, using an iterative procedure. However, the underlying event energy, explained in section 5.1, has a large influence on the measured jet cross sections, as wil be shown below. For relevant conclusions on the photon structure the underlying event has to be well described by the QCD calculation (see Fig.3), or the jet data need to be corrected for underlying event effects (e.g. [4]).

In Fig.6 the inclusive differential jet cross sections $d\sigma/dE_t^{jet}$ and $d\sigma/d\eta^{jet}$ are shown. No corrections for the underlying event energy were applied. Here the rapidity $\eta^{jet}$ in the laboratory system ($\eta - \eta^* = 0.5 \ln (E_p/E_\gamma) \sim 2$) is chosen for compatibility with previous measurements. The cross sections refer to the scaled photon energy $0.25 \leq y \leq 0.7$ and the negative squared momentum transfer below $Q^2 \leq 0.01\,\mathrm{GeV}^2$. The jet transverse energy cross section in Fig.6a was measured in two rapidity intervals $-1 \leq \eta^{jet} \leq 1$ and $-1 \leq \eta^{jet} \leq 2$ (see also tables 1,2). The jet rapidity cross section in Fig.6b was measured for three different threshold in the corrected jet energy $E_t^{jet} \geq 7, 11, 15\,\mathrm{GeV}$ (see also tables 3,4,5).

Corrections to the energy response of the calorimeter were parametrized as functions of the transverse energy and rapidity of the jets. Using generator events the corrections $\epsilon$ result from the comparison between jets resulting from generated hadrons and jets found after a detailed simulation of the detector effects. $\epsilon(E_t^{jet})$ decreases from 1.1 to 0.7 as $E_t^{jet}$ increases between $7 \leq E_t^{jet} \leq 30\,\mathrm{GeV}$. $\epsilon(\eta^{jet})$ decreases from 1.7 to 0.7 with increasing $-1 \leq \eta^{jet} \leq 2$. The uncertainty in the determination of the energy corrections is 10%, including a small dependence on the generator model used. The resolution of the jet parameters was also determined from a comparison of jets from generated hadrons and jets after the detector simulation. The jet transverse energy resolution decreases from about 20% to 10% for jets between 7 and 30 GeV. The resolution in $\eta$ and $\varphi$ was found to be $\sim 0.1$ in the whole $\eta$ range. The hadronic energy resolution is known to the level of 10%. This gives a 10% contribution to the systematic error. The hadronic energy scale of different calorimeter segments is known to be the same to the level of 3%. This results in a 17% error of the cross section. The efficiency of the drift chamber trigger varies as function of $E_t^{jet}$ and $\eta^{jet}$ between 90% and 95%, with an uncertainty of 3%. In Fig.6 the total error bars include the quadratic sum of the statistical and systematic errors mentioned so far.

Sources of systematic errors affecting the cross section normalization are: 1) The dominant systematic error of 28% results from the uncertainty in the knowledge of the LAr energy scale. 2) The error in the luminosity measurement which includes the uncertainty in the electron trigger efficiency is 5%. These errors have been added in quadrature and give a 29% overall systematic error in addition to the errors shown in Fig.6.

The fit to a power law $a(E_t^{jet})^{-n}$ of the jet transverse energy cross section in Fig.6a gives $n = 6.1 \pm 0.5$ for the rapidity interval $-1 \leq \eta^{jet} \leq 2$, where the errors reflect the statistical and systematic uncertainties of the fit. The measured power $n$ is compatible with previous results on jet production in $\gamma p$ interactions [2, 3]. The result compares also well with jet cross sections measured in $\overline{p}p$ collisions at the same cms energy $\sqrt{s_{\overline{p}p}} = 200\,\mathrm{GeV}$ [33] where the same fit function, applied to the same $E_t^{jet}$ range, results in the power $n = -5.8$. This is another demonstration that $\gamma p$ and $\overline{p}p$ hard interactions are – in this kinematic range – predominantly based on the same type of parton scattering processes.

In Fig.6 the calculations of the PYTHIA generator without multiple interactions (dashed curve) are compared with the measured jet cross sections. This model, and also HERWIG without soft underlying event, show clear deficiencies in describing the cross sections of jet production at large rapidities and small transverse energies of the jets. This kinematic region corresponds to events where the momentum fraction of the parton from the photon is small $x_\gamma \sim 0.1$. The dotted line indicates a PYTHIA calculation using another parametrization of the photon structure (LAC1 [34]) which has larger gluon content at small $x_\gamma$ compared to the

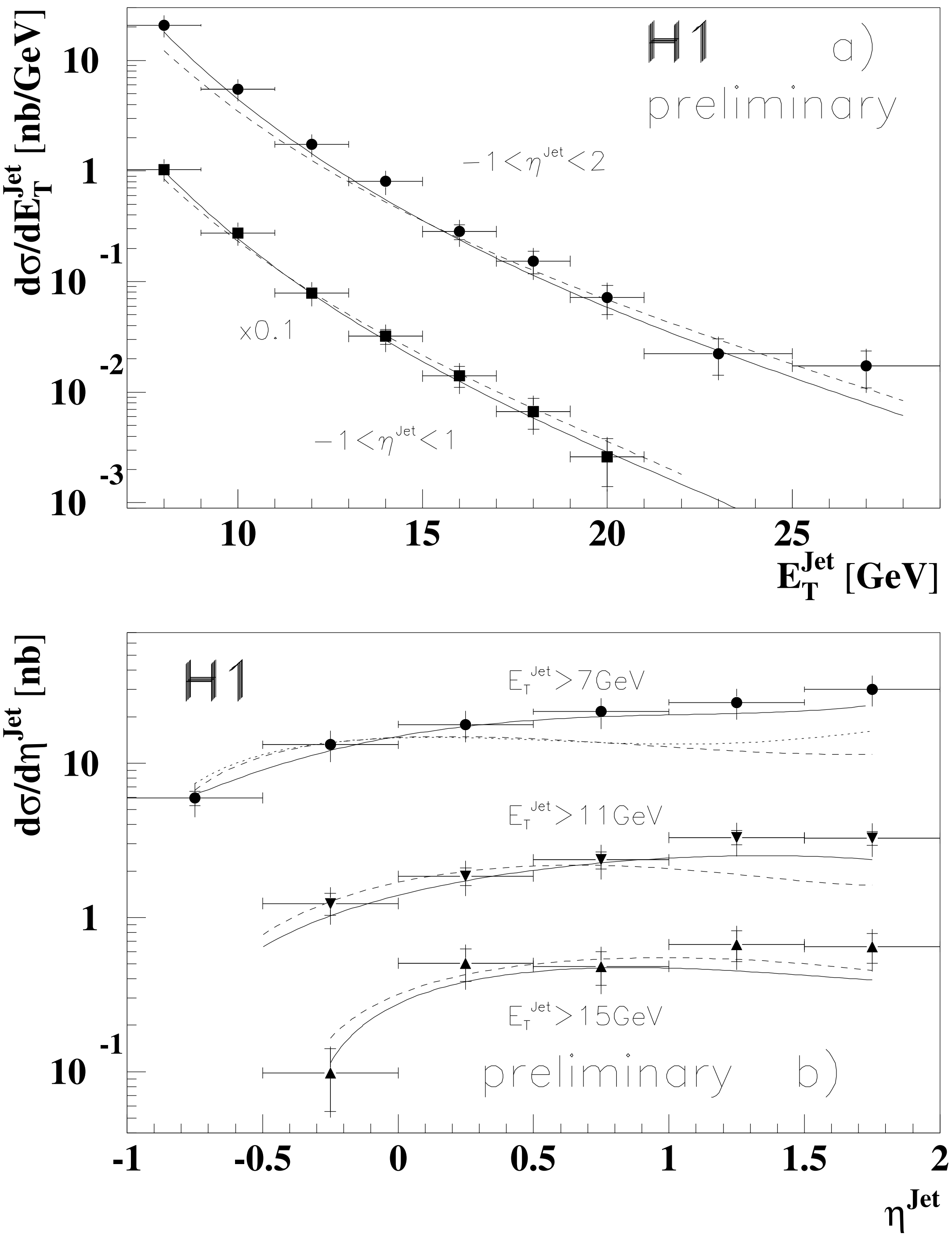


**Figure** 6: a) Inclusive differential jet cross sections for jets with transverse energy above $E_T^{jet} \geq\ 7\,\mathrm{GeV}$ summed in a cone of $R = 1$. Circles are H1 data integrated in the rapidity range $-1 \leq \eta^{jet} \leq 2$, squares refer to the region $-1 \leq \eta^{jet} \leq 1$ (lowered by factor 10). The inner error bars represent the statistical, the outer errors are the quadratic sum of statistical and systematic errors which depend on $E_t^{jet}$ or $\eta^{jet}$. The uncertainty in the overall normalization accounts to 29% and is not shown in the figure. b) Differential jet cross section versus rapidity for different thresholds in the jet transverse energy: circles are H1 data with $E_T^{jet} \geq\ 7\mathrm{GeV}$, down-pointing triangles with $E_T^{jet} \geq\ 11\mathrm{GeV}$, and up-pointing triangles with $E_T^{jet} \geq\ 15\mathrm{GeV}$. The full/dashed curves represent QCD calculations with/without interactions of the beam remnants (PHOJET/PYTHIA). The dotted curve is a calculation using PYTHIA without remnant interactions, but another parametrization of the photon structure function (see text).

parametrization used for the other calculations in this paper (GRV [13]). Also this calculation neither describes the measured energy density (Fig.3), nor the jet cross section measurement.

The full curve represents the calculation of PHOJET generator. The calculations including additional event energy – PHOJET and PYTHIA with multiple interactions – provide a fair description of the shape of the data. The results differ in absolute numbers in the small $E_t^{jet}$ region by factor $\leq 2$ using the same QCD matrix elements and structure functions. However, the calculations include different modeling of 1) the remnant interactions, 2) the transition region to the non-perturbative, soft scattering region, and 3) the parton radiation effects. From the comparisons of these models, conclusions on the parton content in the photon from the measured jet cross sections have, in the low $x_\gamma$ region, an uncertainty of about factor 2.

The distribution of the energy density outside the jets in the central $\gamma p$ collision region $1 \leq \eta \leq 3$ (Fig.3) was used to correct the rapidity jet cross section above $\eta^{jet} \geq 1$ for effects of the underlying event: the difference between the transverse energy density in the data and the PYTHIA calculation without multiple interactions (dashed histogram) indicates the event energy which is produced beyond the hard parton scattering process, its parton showers and their fragmentation effects. This correction lowers the cross section for jets above $E_t^{jet} \geq 7$ GeV by 40%, $E_t^{jet} \geq 11$ GeV by 30%, and $E_t^{jet} \geq 15$ GeV by 15%. These results show, for the first time, the strong influence of the underlying event energy on the jet cross sections.

Table 1: Measured differential $ep$ cross-section $d\sigma/dE_T^{jet}$ for inclusive jet production integrated over $-1.0 \leq \eta^{jet} \leq 2.0$ in the kinematical range defined by $Q^2 < 0.01\ GeV^2$ and $0.25 < y < 0.7$.

| $E_T^{jet}$ $[GeV]$ | $d\sigma/dE_T^{jet}$ $[nb/GeV]$ | $stat.error$ | $syst.error$ | $syst.overall\ error$ |
|---|---|---|---|---|
| 7.0– 9.0 | 20.80 | 0.56 | 4.6 | 5.93 |
| 9.0– 11.0 | 5.51 | 0.26 | 1.2 | 1.57 |
| 11.0– 13.0 | 1.74 | 0.12 | 0.39 | 0.50 |
| 13.0– 15.0 | 0.803 | 0.079 | 0.18 | 0.23 |
| 15.0– 17.0 | 0.283 | 0.044 | 0.063 | 0.081 |
| 17.0– 19.0 | 0.153 | 0.036 | 0.034 | 0.044 |
| 19.0– 21.0 | 0.0715 | 0.021 | 0.016 | 0.020 |
| 21.0– 25.0 | 0.0223 | 0.0081 | 0.0050 | 0.0063 |
| 25.0– 29.0 | 0.0172 | 0.0063 | 0.0038 | 0.0049 |

**Summary**

The width of jets in photoproduction is measured to decrease with increasing jet energy. This change of the jet shape is expected from QCD calculations and can be explained by parton radiation effects. Comparisons of jet width, measured in $\gamma p$ and $\overline{p}p$ scattering, show that these jets are of a common nature.

Table 2: Measured differential $ep$ cross-section $d\sigma/dE_T^{jet}$ for inclusive jet production integrated over $-1.0 \leq \eta^{jet} \leq 1.0$ in the kinematical range defined by $Q^2 < 0.01\ GeV^2$ and $0.25 < y < 0.7$.

| $E_T^{jet}$ $[GeV]$ | $d\sigma/dE_T^{jet}$ $[nb/GeV]$ | $stat.error$ | $syst.error$ | $syst.overall\ error$ |
|---|---|---|---|---|
| 7.0– 9.0 | 10.33 | 0.39 | 2.36 | 3.09 |
| 9.0– 11.0 | 2.76 | 0.19 | 0.63 | 0.83 |
| 11.0– 13.0 | 0.787 | 0.078 | 0.18 | 0.24 |
| 13.0– 15.0 | 0.322 | 0.049 | 0.074 | 0.096 |
| 15.0– 17.0 | 0.141 | 0.030 | 0.032 | 0.042 |
| 17.0– 19.0 | 0.0672 | 0.021 | 0.015 | 0.020 |
| 19.0– 21.0 | 0.0263 | 0.012 | 0.0060 | 0.0079 |

Table 3: Measured differential $ep$ cross-section $d\sigma/d\eta^{jet}$ for inclusive jet production integrated over $E_T^{jet} > 7.0\ GeV$ in the kinematical range defined by $Q^2 < 0.01\ GeV^2$ and $0.25 < y < 0.7$.

| $\eta^{jet}$ | $d\sigma/d\eta^{jet}$ $[nb]$ | $stat.error$ | $syst.error$ | $syst.overall\ error$ |
|---|---|---|---|---|
| -1.0 - -0.5 | 5.94 | 0.64 | 1.32 | 1.69 |
| -0.5 - 0.0 | 13.18 | 0.86 | 2.93 | 3.76 |
| 0.0 - 0.5 | 17.81 | 1.05 | 3.95 | 5.08 |
| 0.5 - 1.0 | 21.58 | 1.14 | 4.79 | 6.15 |
| 1.0 - 1.5 | 24.80 | 1.16 | 5.51 | 7.07 |
| 1.5 - 2.0 | 30.11 | 1.33 | 6.68 | 8.58 |

Jet cross sections are measured depending on the jet transverse energy and rapidity. Both are well described by LO QCD calculations which include in addition to the matrix elements of the parton scattering processes parton showers and interactions of the beam spectators. The strong influence of the underlying event energy on the measured jet cross sections are demonstrated, and give rise to factor 2 uncertainties in the conclusions on the parton scattering processes.

# 7 Conclusions

High $E_t$ $\gamma p$ collision events show similar characteristics in the energy distributions and jet production as observed in hadron-hadron scattering. The comparison with models supports a scenario with secondary interactions of the beam remnants added to the model based on LO QCD calculations to describe observed characteristics of the underlying event in $\gamma p$ collisions. In absence of model based on full NLO QCD calculations we can not however exclude that the observed underlying event characteristics are consistently described by NLO QCD calculations.

The energy of this underlying event influences measured jet cross sections strongest in the region of small jet transverse energies $E_t^{jet} \sim 7$ GeV and large rapidities $\eta^{jet} \geq 1$, the kinematic

Table 4: Measured differential $ep$ cross-section $d\sigma/d\eta^{jet}$ for inclusive jet production integrated over $E_T^{jet} > 11.0\ GeV$ in the kinematical range defined by $Q^2 < 0.01\ GeV^2$ and $0.25 < y < 0.7$.

| $\eta^{jet}$ | $d\sigma/d\eta^{jet}$ [nb] | stat.error | syst.error | syst.overall error |
|---|---|---|---|---|
| -0.5 - 0.0 | 1.23 | 0.20 | 0.27 | 0.35 |
| 0.0 - 0.5 | 1.85 | 0.24 | 0.41 | 0.53 |
| 0.5 - 1.0 | 2.36 | 0.30 | 0.52 | 0.67 |
| 1.0 - 1.5 | 3.30 | 0.35 | 0.73 | 0.94 |
| 1.5 - 2.0 | 3.27 | 0.33 | 0.73 | 0.93 |

Table 5: Measured differential $ep$ cross-section $d\sigma/d\eta^{jet}$ for inclusive jet production integrated over $E_T^{jet} > 11.0\ GeV$ in the kinematical range defined by $Q^2 < 0.01\ GeV^2$ and $0.25 < y < 0.7$.

| $\eta^{jet}$ | $d\sigma/d\eta^{jet}$ [nb] | stat.error | syst.error | syst.overall error |
|---|---|---|---|---|
| -0.5 - 0.0 | 0.098 | 0.043 | 0.02 | 0.028 |
| 0.0 - 0.5 | 0.504 | 0.12 | 0.11 | 0.14 |
| 0.5 - 1.0 | 0.482 | 0.12 | 0.11 | 0.14 |
| 1.0 - 1.5 | 0.668 | 0.15 | 0.15 | 0.19 |
| 1.5 - 2.0 | 0.645 | 0.14 | 0.14 | 0.18 |

region which corresponds to small momentum fractions $x_\gamma$ of the parton from the photon. Conclusions on the parton scattering processes at small $x_\gamma$ from the jet cross sections therefore depend on the description of the underlying event energy.

# References


[1] W. J. Stirling, "Proceedings of the HERA Workshop", ed.R.D.Peccei, Hamburg 1987 and references therein

[2] H1 Collab., I. Abt et al., Phys. Lett. B314 (1993) 436

[3] ZEUS Collab., M. Derrick et al., Phys. Lett. B342 (1995) 417

[4] H1 Collab., T. Ahmed et al., DESY-95-062

[5] S.D.Ellis, Proceedings "QCD and High Energy Hadronic Interactions", 28th Rencontre de Moriond, Ed. J. Tran Thanh Van, Editions Frontieres (1993) 235

[6] T. Sjöstrand and M. van Zijl, Phys. Rev. D36 (1987) 2019

[7] H1 Collab., I. Abt et al., "The H1 detector at HERA", DESY preprint 93-103 (1993), to be submitted to Nucl. Instr. and Meth.

[8] H1 Calorimeter Group, B. Andrieu et al., Nucl. Instr. and Meth. A336 (1993) 460

[9] H1 Calorimeter Group, B. Andrieu et al., Nucl. Instr. and Meth. A350 (1994) 57

[10] H1 Calorimeter Group, B. Andrieu et al., Nucl. Instr. and Meth. A336 (1993) 499

[11] J. E. Huth et al., FERMILAB-CONF-90/249-E (1990)

[12] M. Glück, E. Reya and A. Vogt, Z. Phys. C53 (1992) 127

[13] M. Glück, E. Reya and A. Vogt, Phys. Rev. D46 (1992) 1973

[14] T. Sjöstrand, CERN-TH-6488 (1992), Comput. Phys. Commun. 82 (1994) 74

[15] G. Schuler and T. Sjostrand, Nucl. Phys. B407 (1993) 539

[16] UA2 Collab., J.Alitti et.al. Phys. Lett. B268 (1991) 145

[17] AFS Collab., T. Akesson et al., Z. Phys. C34 (1987) 163

[18] CDF Collab. L.J. Keeble et al., FERMILAB-CONF-92-161-E (1992)

[19] T. Sjöstrand, M. Bengtsson, Comput. Phys. Commun. 43 (1987) 367

[20] G. Marchesini, et al., Comput. Phys. Commun. 67 (1992) 465

[21] G. Marchesini and B.R. Webber, Nucl. Phys. B310 (1988) 461
G. Marchesini and B.R. Webber, Nucl. Phys. B238 (1984) 1

[22] B.R. Webber, Nucl. Phys. B238 (1984) 492
G. Marchesini and B.R. Webber, Phys. Rev. D38 (1988) 3419

[23] A. Capella et al., Phys. Rep. 236 (1994) 227

[24] P. Aurenche et al., Phys. Rev. D45 (1992) 92
F.W. Bopp et al., Comp. Phys. Commun. 83 (1994) 107

[25] A. Capella et al., Phys. Rev. Lett. 58 (1987) 2015

[26] R. Engel, Z. Phys. C66 (1995) 203

[27] ZEUS Collab., M. Derrick et al., Phys. Lett. B297 (1992) 404

[28] AFS Collab., T. Akesson et al., Phys. Lett. B128 (1983) 354

[29] P. Capiluppi et al., Nucl. Phys. B70 (1974) 1
BS Collab., B. Alper et al., Nucl. Phys. B100 (1975) 237

[30] UA1 Collab., C. Albajar et al., Z. Phys. C36 (1987) 33

[31] CDF Collab., F. Abe et al., Phys. Rev. D45 (1992) 2249

[32] S.D. Ellis, J. Phys. G, Nucl. Part. Phys. 17 (1991) 1552

[33] UA1 Collab., C. Albajar et al., Nucl. Phys. B309 (1988) 405

[34] H. Abramowicz, K. Charchula, A. Levy, Phys. Lett. B269 (1991) 458

[35] UA1 Collab., G.Arnison et al., Phys. Lett. B132 (1983) 214

[36] G. Kramer, S.G. Salesch, Z. Phys. C61 (1994) 277
D. Bödeker, G. Kramer, S.G. Salesch, Z. Phys. C63 (1994) 471

[37] G.Kramer und S.G.Salesch, Phys. Lett. B317 (1993) 218
S.G.Salesch, DESY 93-196 (1993)
G.Kramer und S.G.Salesch, Phys. Lett. B333 (1994) 519

[38] M. Klasen and S.G. Salesch, calculations based on [36] (1994)